Nanoscale Surface Topography and Growth of Molecular Crystals: The Role of Anisotropic Intermolecular Bonding

Phillip W. Carter, Andrew C. Hillier, and Michael D. Ward*

Contribution from the Department of Chemical Engineering and Materials Science, University of Minnesota, Amundson Hall, 421 Washington Avenue SE, Minneapolis, Minnesota 55455

Received August 23, 1993. Revised Manuscript Received November 1, 1993®

Abstract: Atomic force microscopy (AFM) and phase measurement interferometric microscopy (PMIM) of the molecular crystals α-glycine and $(TMTSF)_2ClO_4$ (TMTSF = tetramethyltetraselenafulvalene) reveal that crystal topography, growth, and etching reflect the relative strengths of solid state intermolecular bonding. The (010), (110), and (011) faces of α-glycine exhibit terraces, ledges, and kinks that can be interpreted on the basis of intermolecular hydrogen bonding in these planes. A strong preference for [100] ledges on the (001) face of $(TMTSF)_2ClO_4$ is a consequence of strong intermolecular charge transfer interactions between TMTSF molecules stacked along this direction. Dynamic *in situ* measurements of growth and etching indicate that the topographic structure is formed and preserved during these active processes. AFM studies of crystal growth and etching of $(TMTSF)_2ClO_4$ are particularly convenient, as these processes can be controlled through adjustment of the electrochemical potential applied to single crystals. In this case, layer-by-layer growth or etching, in which the layers correspond to single unit cell heights, occurs by a terrace–ledge–kink mechanism with the direction of fastest growth or etching oriented along the TMTSF stacking axis. In both α-glycine and $(TMTSF)_2ClO_4$, the nanoscale topographic structure resembles the macroscopic morphology, suggesting self-similarity across the length scales examined. The role of excess interfacial energy during crystal growth is evident from the distributions of terraces, ledges, and kinks, which differ from those observed under equilibrium conditions.

Introduction

Molecular crystals, which comprise crystalline solids based upon molecular components, exhibit a variety of fundamentally interesting and technologically important properties, including solid-state reactivity, conductivity, superconductivity, nonlinear optical behavior, and ferromagnetism.[1] Many pharmaceutical reagents also derive from this class of materials.[2] The considerable interest in molecular crystals stems from the potential for rational design of their bulk properties through manipulation of the molecular substituents and supramolecular solid-state structure, a strategy commonly referred to as "crystal engineering."[3] While there has been considerable study of the intermolecular interactions that direct solid-state packing in molecular crystals, investigations of their nucleation and growth, particularly at the molecular level, have been rather limited.[4-7] An understanding of these processes, particularly at the nanoscopic level, is crucial in order to address issues of size, purity, growth orientation, defect density, and polymorphism in molecular crystals.

The growth of a molecular crystal can be described as a stepwise self-assembly process whereby molecules form prenucleation aggregates, which evolve into nuclei and further grow into macroscopic crystals.[8] A particularly useful description of crystal growth in this regard is the terrace–ledge–kink (TLK) model,[9] which involves a series of elementary steps, including surface diffusion of molecules or aggregates and their attachment to topographic features such as terraces, ledges, or kinks.[10] The importance of each elementary step depends not only upon their relative rates but also upon the distribution and reactivity of these features. It therefore is important to examine the factors that influence the existence of these topographic features, their relationship to intermolecular solid-state interactions, and their dependence upon the excess interfacial energy that is typically present during crystal growth.[11] While many of these characteristics have been surmised from macroscopic crystal growth rates and morphologies,[12] at nanoscopic length scales crystal morphologies and topographic features may be influenced more strongly by surface energetics than by bulk lattice energies.

The need to obtain detailed characterization of crystal interfaces and to understand the role of topographic features in crystal

* Author to whom correspondence should be addressed.

® Abstract published in *Advance ACS Abstracts*, January 1, 1994.

(1) (a) Miller, J. S. *Extended Linear Chain Compounds;* Plenum: New York, 1982–84; Vols. 1–3. (b) Miller, J. S.; Epstein, A. J.; Reiff, W. M. *Science* **1988**, *240*, 40. (c) Garito, A. F.; Heeger, A. J. *Acc. Chem. Res.* **1974**, *7*, 232. (d) Torrance, J. B. *Acc. Chem. Res.* **1979**, *12*, 79.

(2) Byrn, S. R. *Solid State Chemistry of Drugs*; Academic Press: New York, 1982.

(3) (a) Schmidt, G. M. J. *Pure Appl. Chem.* **1971**, *27*, 647. (b) Lehn, J. M. *Angew. Chem., Int. Ed. Engl.* **1988**, *27*, 89. (c) Desiraju, G. *Crystal Engineering—The Design of Organic Solids*; Elsevier; New York, 1989. (d) Fagan, P. J.; Ward, M. D.; Calabrese, J. C. *J. Am. Chem. Soc.* **1989**, *111*, 1698. (e) Ward, M. D.; Fagan, P. J.; Calabrese, J. C.; Johnson, D. C. *J. Am. Chem. Soc.* **1989**, *111*, 1698.

(4) (a) Mobus, M.; Schreck, M.; Karl, N. *Thin Solid Films* **1989**, *175*, 89. (b) Yanagi, H.; Takemoto, K.; Hayashi, S.; Ashida, M. *J. Cryst. Growth* **1990**, *99*, 1038. (c) Hayashi, S.; Ikuno, H.; Yanagi, H.; Ashida, M. *J. Cryst. Growth* **1992**, *123*, 35. (d) Zimmerman, U.; Schnitzler, G.; Karl, N.; Umbach, E.; Dudde, R. *Thin Solid Films* **1989**, *175*, 85.

(5) (a) Popovitz-Biro, R.; Lahav, M.; Leiserowitz, L. *J. Am. Chem. Soc.* **1991**, *113*, 8943. (b) Gavish, M.; Popovitz-Biro, R.; Lahav, M.; Leiserowitz, L. *Science* **1990**, *250*, 973. (c) Gavish, M.; Wang, J.-L.; Eisenstein, M.; Lahav, M.; Leiserowitz, L. *Science* **1992**, *256*, 815. (d) Landau, E. M.; Grayer Wolf, S.; Levanon, M.; Leiserowitz, L.; Lahav, M.; Sagiv, J. *J. Am. Chem. Soc.* **1989**, *111*, 1436. (e) Addadi, L.; Berkovitch-Yellin, Z.; Weissbuch, I.; van Mil, J.; Shimon, L. J. W.; Lahav, M.; Leiserowitz, L. *Angew. Chem., Int. Ed. Engl.* **1985**, *24*, 466.

(6) Carter, P. W.; Ward, M. D. *J. Am. Chem. Soc.* **1993**, *115*, 11521.

(7) Weissbuch, I.; Addadi, L.; Lahav, M.; Leiserowitz, L. *Science* **1991**, *253*, 637.

(8) Addadi, L.; Berkovitch-Yellin, Z.; Weissbuch, I.; van Mil, J.; Shimon, L. J. W.; Lahav, M.; Leiserowitz, L. *Angew. Chem., Int Ed. Engl.* **1985**, *24*, 466.

(9) Tiller, W. A. *The Science of Crystallization: Microscopic Interfacial Phenomena*; Cambridge University Press: New York, 1991, pp 327–381.

(10) (a) Bennema, P.; Gilmer, G. in *Crystal Growth: An Introduction*; Hartman, P., Ed.; North Holland: Amsterdam, The Netherlands, 1973; p 272. (b) Elwenspoek, M.; Bennema, P.; van der Eerden, J. P. *J. Cryst. Growth* **1987**, *83*, 297. (c) Bennema, P.; van der Eerden, J. P. *Morphology of Crystals*; Terra Scientific Publishing Co.: Tokyo, 1987; pp 1–75. (d) Bourne, J. R.; Davey, R. *J. Cryst. Growth* **1976**, *36*, 278. (e) Bourne, J. R.; Davey, R. *J. Cryst. Growth* **1976**, *36*, 287.

(11) Hartman, P. In *Crystal Growth: An Introduction*; Hartman, P., Ed.; North Holland: Amsterdam, The Netherlands, 1973; p 367.

(12) Berkovitch-Yellin, Z. *J. Am. Chem. Soc.* **1985**, *107*, 8239.

0002-7863/94/1516-0944$04.50/0

growth has prompted us to examine the nucleation and growth of molecular crystals, *in situ*, with atomic force microscopy (AFM)[13] and phase measurement interferometric microscopy (PMIM).[14] While previous reports have indicated that AFM can be used to obtain contour images of the surfaces of organic films and organic crystals,[15] examination of crystal *growth* with this technique has been limited to inorganic crystals,[16] amino acids,[17] and the protein lysozyme.[18] The goal of our studies has been to probe the morphology, interfacial structure, nucleation, and growth of molecular crystals at the nanoscale level and to establish the relationships between these properties and solid-state *intermolecular* interactions. We present herein investigations of crystalline systems whose solid-state structures have anisotropic intermolecular bonding due to strong hydrogen-bonding or charge-transfer interactions. Specifically, we describe *in situ* studies of the dynamic growth of α-glycine and $(TMTSF)_2ClO_4$ (TMTSF = tetramethyltetraselenafulvalene) that demonstrate the relationship of intermolecular bonding to topographic features and crystal growth mechanisms at the nanoscale level.

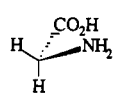

glycine

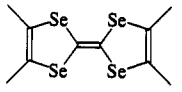

TMTSF

Experimental Section

Apparatus. Atomic force microscopy (AFM) experiments were performed with a Digital Instruments Nanoscope III scanning probe microscope equipped with Nanoprobe cantilevers (Si_3N_4 integral tips with spring constants of 0.3 and 0.06 nm^{-1}, PARK Scientific). Images were obtained in the constant force mode with filters off, an integral gain of 3.0, a proportional gain of 7.0, and a look-ahead gain of 0.0. The tip scan rate during image acquisition ranged from 5 to 30 Hz, with higher scan rates increasing feedback noise as well as increasing mechanical etching of the crystal surfaces. Both "d" and "j" scan heads were used, having maximum scan ranges of 12 × 12 × 4.4 μm^3 and 125 × 125 × 5 μm^3, respectively. The applied tip–sample force was generally 20–50 nN in air and was ≤10 nN in solution. Damage to the crystal surfaces was minimized by employing small tip forces, slow scan rates, and operation of the microscope in calibration mode when images were not being acquired. In order to minimize tip-induced surface damage and etching of the crystals,[19] the applied force was reduced by lowering the setpoint voltage (tip deflection).

In situ AFM studies of α-glycine crystals were performed at room temperature in an aqueous solution near supersaturation conditions. The crystals were mounted with epoxy onto a magnetic stainless steel disk having a centered cylindrical trough. An AFM fluid cell (Digital Instruments), comprising a quartz body with ports for fluid entry and exit, was sealed to the disk with an O-ring. *In situ* AFM studies of $(TMTSF)_2ClO_4$ were performed after mounting a mature single crystal with conductive silver epoxy (EpoTek) onto a stainless steel disk such that the (001) face was exposed. The crystal was aligned with its [100] needle axis parallel to the AFM vertical scan direction (*y*-axis). An AFM electrochemical fluid cell (Digital Instruments) was employed in a three-electrode configuration with the $(TMTSF)_2ClO_4$ as the working electrode and platinum and silver wires as counter and quasi-reference electrodes, respectively. The counter and reference electrodes were placed in the outlet port of the fluid cell. Etching experiments were performed in either ethanol or propylene carbonate containing 0.1 M n-Bu_4N^+-ClO_4^-. Growth experiments were performed in propylene carbonate containing 0.1 M n-$Bu_4N^+ClO_4^-$ and saturated with TMTSF (approximately 1 mM).

Phase measurement interferometric microscopy (PMIM) was performed with a Zygo Maxim-3D Model 5700 Noncontact Surface Profiler (Zygo Corporation, Middlefield, CT 06455). Crystal surfaces were examined *in situ* using a teflon cell with a glass window sealed to a teflon O-ring with a screw clamp. A 40× Mirau objective was used, which provided an overall 640× magnification power and an imaging area of 245 μm × 245 μm with a lateral resolution of 0.77 μm. The objective was approximately 1 mm from the glass window and 4 mm from the substrate crystal surface. Experiments with α-glycine were performed in saturated aqueous solutions introduced to the cell with a syringe. The cell was sealed to avoid evaporation of the water. The refractive index of the saturated glycine solutions was approximately $\eta_{gly} = 1.38$, which limited the maximum resolvable vertical step height to 114 nm. The vertical resolution was approximately 4 Å. Details of instrumentation and PMIM analysis have been presented elsewhere.[14]

Single crystals of α-glycine and $(TMTSF)_2ClO_4$ were indexed for assignment of crystallographic planes with an Enraf-Nonius CAD-4 X-ray diffractometer using Mo Kα radiation. The measured lattice parameters were in agreement with reported values. X-ray indexing was especially important in the case of α-glycine. Although crystallographic assignments generally could be made by simple inspection of the α-glycine crystal morphology, the long axis of the (010) face *did not* always correspond to the crystallographic *c* axis.

Materials. Single crystals of α-glycine (>99%, Aldrich) were grown by slow evaporation of saturated aqueous solutions. The {010}, {110}, and {011} faces were the most well-developed of the bipyramidal crystals, in agreement with literature reports of the crystal morphology.[21] Fresh {010} faces were exposed by cleaving, while {110} and {011} surfaces were studied using as-grown crystals. Crystals of 5–10-mm dimensions were used for surface microscopy studies. Single crystals of $(TMTSF)_2ClO_4$ were grown in a conventional H-cell by electrochemical oxidation of TMTSF (5 mM TMTSF, Aldrich) at a platinum wire electrode (250 μm × 10 mm) in a methylene chloride solution containing 0.1 M n-Bu_4N^+-ClO_4^- (Sigma). Crystals were grown for a period of 1–4 days at an applied current of 1 μA (2.0 mA cm^{-2}). Mature crystals possessed a needle habit (5 × 1 x 0.1 mm^3) with the largest face identified as (001) and the needle axis parallel to [100].

Results

Defining Topographic Features. In order to interpret AFM and PMIM images of crystal faces and dynamic growth and etching processes on those faces, it is useful to define the topographic features that play an important role in crystal growth (Figure 1). Ledges are described by the intersection of a terrace plane and a step plane, and are designated by the crystallographic *direction* of the intersection line. These ledges will have a characteristic repeat distance, referred to as $\lambda_{(hkl)}$. Attachment of molecules or aggregates to ledges results in the formation of kinks upon which growth occurs parallel to the ledge, a process which is more favorable than the initial aggregate ledge attachment. The formation of kink sites is synonymous with the

(13) Binnig, G.; Quate, C. F.; Gerber, Ch. *Phys. Rev. Lett.* **1986**, *56*, 930.
(14) (a) Smith, C. P.; Fritz, D. C.; Tirrell, M.; White, H. S. *Thin Solid Films* **1991**, *198*, 369. (b) Tolansky, S. *Surface Microtopography*; Interscience Publishers, Inc.: New York, 1960. (c) Tolansky, S. *Multiple-Beam Interferometry of Surfaces and Films*; Dover Publications, Inc.: New York, 1970.
(15) (a) Frommer, J. *Angew. Chem., Int. Ed. Engl.* **1992**, *31*, 1298 and references therein. (b) Overney, R. M.; Howald, L.; Frommer, J.; Meyer, E.; Brodbeck, D.; Guntherodt, H.-J. *Ultramicroscopy* **1992**, *42–44*, 983. (c) Gould, S.; Marti, O.; Drake, B.; Hellemans, L.; Bracker, C. E.; Hansma, P. K.; Keder, N. L.; Eddy, M. M.; Stucky, G. D. *Nature* **1988**, *332*, 332. (d) Littke, W.; Haber, M.; Guntherodt, H.-J. *J. Cryst. Growth* **1992**, *122*, 80. (e) Magonov, S. N.; Bar, G.; Gorenberg, A. Y.; Yagubskii, E. B.; Cantow, H.-J. *Adv. Mater.* **1993**, *5*, 453.
(16) (a) Hillner, P. E.; Gratz, A. J.; Manne, S.; Hansma, P. K. *Geology* **1992**, *20*, 359. (b) Hillner, P. E.; Manne, S.; Gratz, A. J.; Hansma, P. K. *Ultramicroscopy* **1992**, *42–44*, 1387. (c) Gratz, A. J.; Manne, S.; Hansma, P. K. *Science* **1991**, *251*, 1343.
(17) Manne, S. J.; Cleveland, J. P.; Stucky, G. D.; Hansma, P. K. *J. Cryst. Growth* **1993**, *130*, 333.
(18) Durbin, S. D.; Carlson, W. E. *J. Cryst. Growth* **1992**, *122*, 71.
(19) (a) Jung, T. A.; Moser, A.; Hug, H. J.; Brodbeck, D.; Hofer, R.; Hidber, H. R.; Schwarz, U. D. *Ultramicroscopy* **1992**, *42–44*, 1446. (b) Delawski, E. J.; Parkinson, B. A. *J. Am. Chem. Soc.* **1992**, *114*, 1661. (c) Hamada, E.; Kaneko, R. *Ultramicroscopy* **1992**, *42–44*, 184. (d) Bosbach, D.; Rammensee, W. *Ultramicroscopy* **1992**, *42–44*, 973. (e) Brumfield, J. C.; Goss, C. A.; Irene, E. A.; Murray, R. W. *Langmuir* **1992**, *8*, 2810. (f) Kim, Y.; Lieber, M. *Science* **1992**, *257*, 375. (g) Meyer, E.; Howald, L.; Overney, R.; Brodbeck, D.; Luthi, R.; Haefke, H.; Frommer, J.; Guntherodt, H.-J. *Ultramicroscopy* **1992**, *42–44*, 274.
(20) Reference deleted in press.
(21) Weissbuch, I.; Addadi, L.; Berkovitch-Yellin, Z.; Gati, E.; Weinstein, S.; Lahav, M.; Leiserowitz, L. *J. Am. Chem. Soc.* **1983**, *105*, 6615.

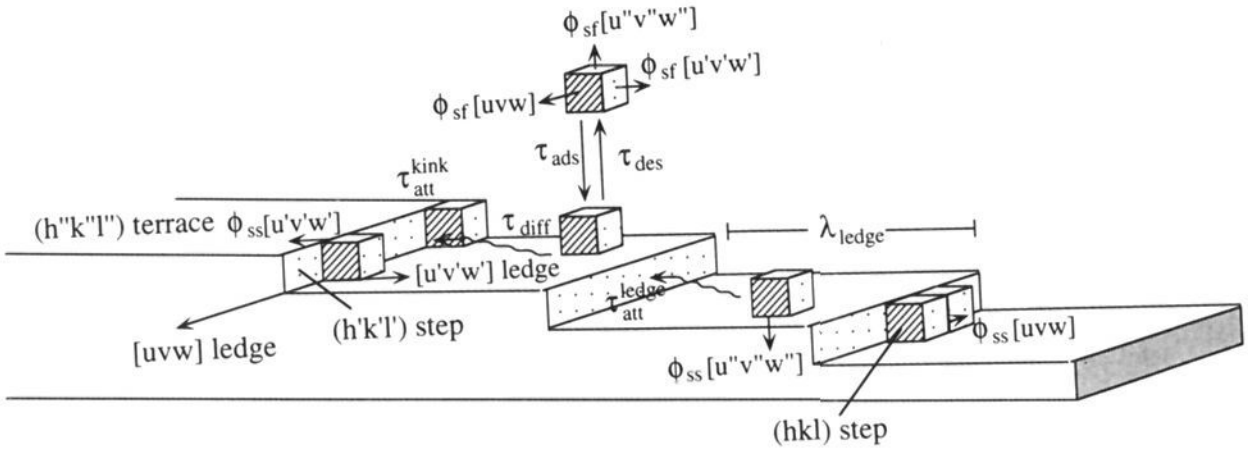

Figure 1. Schematic representation of topographic features on a hypothetical crystal interface. The interface consists of ($h''k''l''$) terraces and (hkl) and ($h'k'l'$) step planes. The intersections of step planes and the terrace constitute a ledge, which is defined by its crystallographic direction. The introduction of a kink site also results in the formation of a new ledge (defined here as [$u'v'w'$]). Crystal growth depends upon the identity and number of ledges and kinks, the strength of intermolecular bonding along specified crystallographic directions (ϕ_{ss}[uvw]), and the interaction of the crystal planes with the fluid (ϕ_{sf}[uvw]). The periodicity of the ledges is defined by a wavelength, λ_{ledge}. The τ values represent the time scale for some of the key elementary steps, such as adsorption, desorption, surface diffusion, and ledge and kink attachment. The blocks depicted in the figure represent molecular aggregates. The actual planes and directions corresponding to the schematic are given in Table 1.

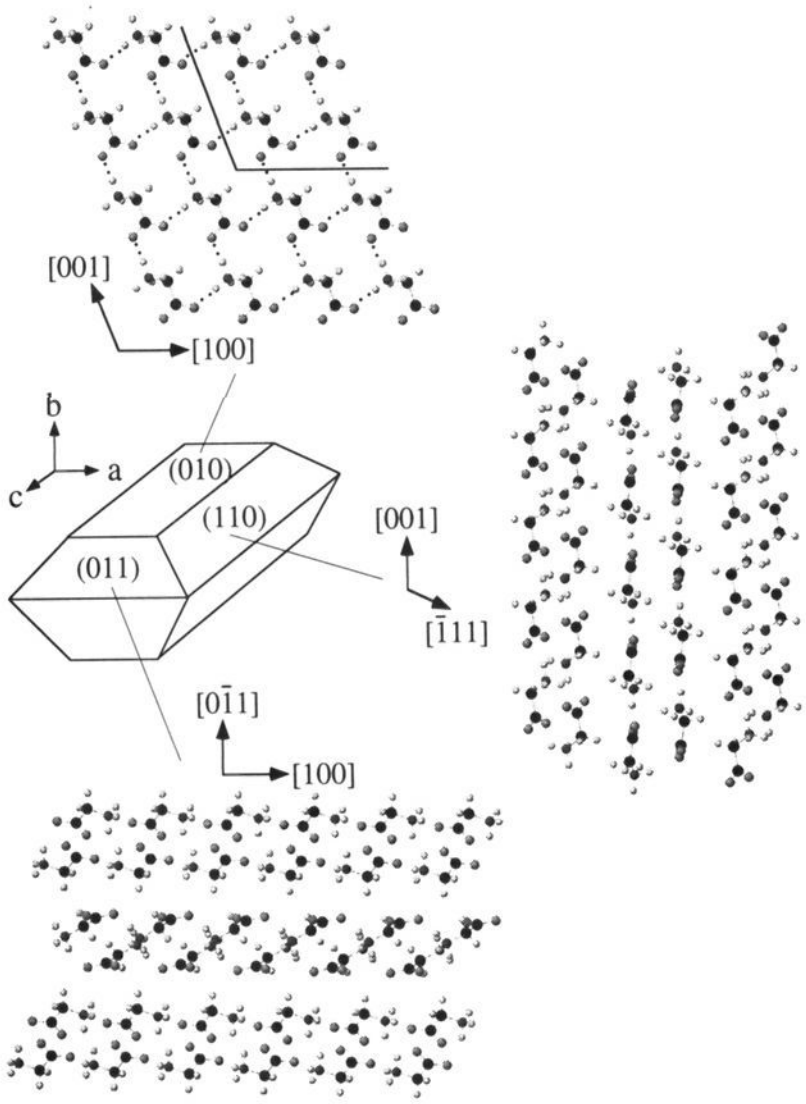

Figure 2. Schematic representation of the macroscopic crystal habit of α-glycine obtained from aqueous solution. The molecular structure of the {010}, {110}, and {011} faces is also illustrated. Hydrogen-bonded {010} sheets pack into bilayers. Glycine molecules form strong hydrogen bonds (dotted contacts) within the {010} sheet. N–H···O contacts of 2.76 and 2.88 Å separate glycine molecules along [001] and [100], respectively. The [001] and [100] ledge directions forming the observed kink sites are shown by solid lines. Hydrogen-bonded chains are readily observed in the molecular structures of the {011} and {110} faces.

introduction of a new [$u'v'w'$] ledge extending from the original [uvw] ledge. Repeated construction of a ledge by kink coalescence in this manner results in ledge advancement orthogonal to its direction, although the normal growth velocity is actually smaller than that of kink advancement along the ledge. According to this description, growth normal to a terrace actually occurs by a layering mechanism involving sequential advancement of these ledges. The examples given below illustrate the relationships between anisotropic intermolecular bonding and the *nanoscale* topography, growth, and etching of specific crystal faces.

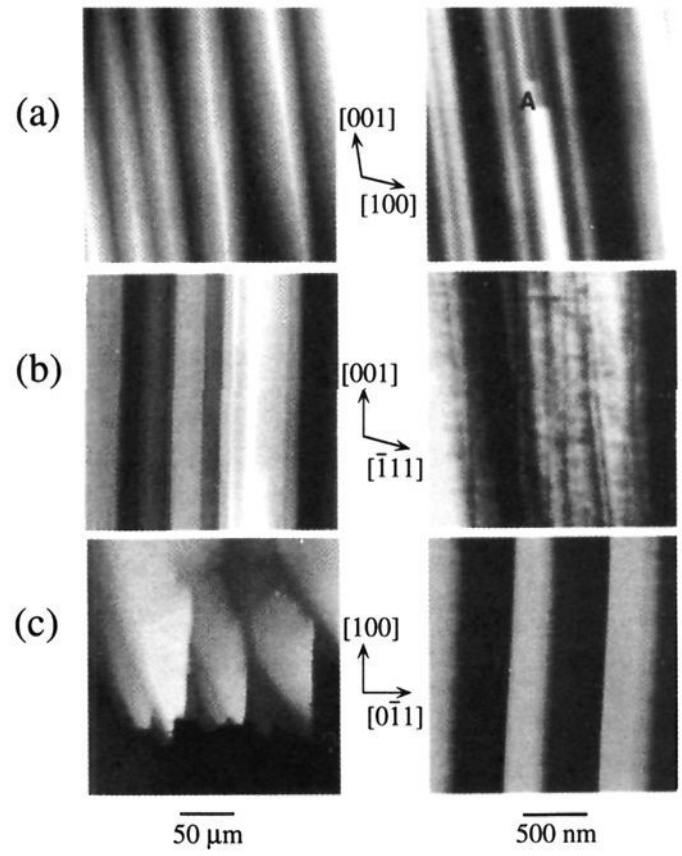

Figure 3. Surface structures of α-glycine crystal faces in aqueous 3.5 M glycine solutions as characterized by *in situ* PMIM (left) and *in situ* AFM (right): (a) {010} face; (b) {110} face; (c) {011} face. The vertical scales are approximately 1000 and 100 nm for the PMIM and AFM images, respectively. The ledge directions are coincident with the strongest hydrogen bonded axis within the crystal plane. The PMIM image of {011} illustrates the shape of advancing terraces during growth at high supersaturations. The AFM data were obtained in the constant-force mode and are unfiltered.

α-Glycine. α-Glycine crystallizes from aqueous solutions in the monoclinic space group $P2_1/n$ (a = 5.102, b = 11.971, c = 5.457 Å, and β = 111.7°).[22] The crystals are bipyramidal, with the {110} and {011} family of planes comprising the eight side faces of the crystal bipyramid, with {010} planes capping the ends (Figure 2). The X-ray crystal structure reveals glycine molecules packed into hydrogen-bonded sheets within the (010) plane. Each (010) sheet is characterized by N···O contacts of 2.76 and 2.88 Å between molecules along the crystallographic c ([001]) and a ([100]) axes, respectively (the crystallographic directions and planes will herein be referred to by the general notations [hkl] and (hkl), respectively). The (010) sheets are organized into a bilayer structure that is enforced by strong electrostatic and hydrogen-bonding (two N···O contacts of 2.93 and 3.05 Å between sheets) interactions between zwitterionic glycine molecules.

(22) (a) Albrecht, G.; Corey, R. B. *J. Am. Chem. Soc.* **1939**, *61*, 1087. (b) Power, L. F.; Turner, K. E.; Moore, F. H. *Acta. Cryst. B* **1976**, *32*,11.

Table 1. Active Ledges and Step Planes Observed in the Growth of α-Glycine and $(TMTSF)_2ClO_4$

	fastest growth direction		next fastest growth direction	
crystal face	$[uvw]^b$	probable (hkl) step plane[a]	$[u'v'w']^b$	probable $(h'k'l')$ step plane[a]
α-glycine				
(010)	[001]	(011)	[100]	(110)
(110)	[001]	(011)	$[\bar{1}11]$	(010) or $(\bar{1}10)$
(011)	[100]	unidentified	$[0\bar{1}1]$	(010) or $(0\bar{1}1)$
$(TMTSF)_2ClO_4$				
(001)	[100]	(210)	$[\bar{1}20]$	(010)

[a] Probable step planes are assigned on the basis of their parallelism with the ledge direction and morphological importance in macroscopic crystals. [b] The convention for growth directions and planes is depicted in Figure 1.

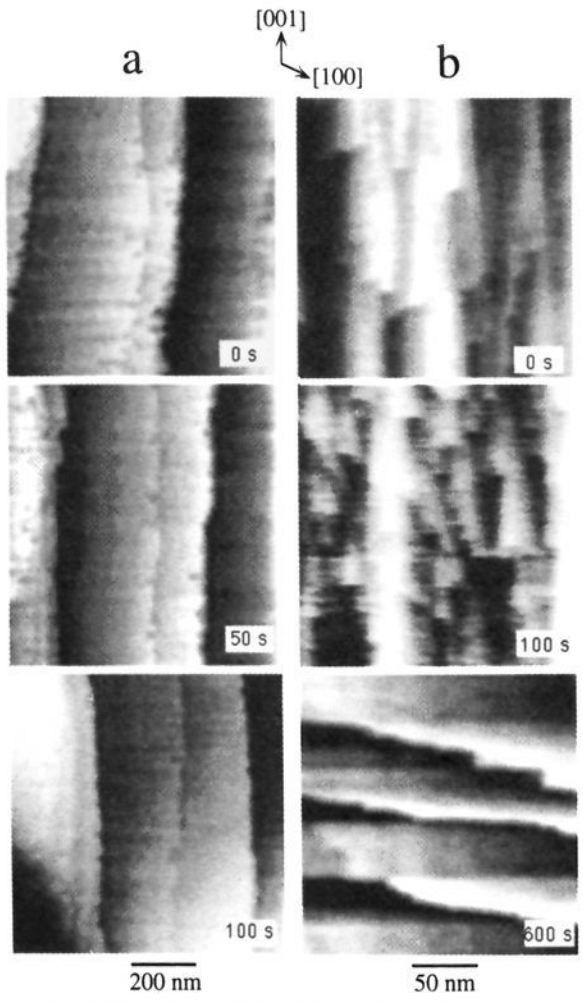

Figure 4. *In situ* AFM of the {010} face of α-glycine in supersaturated aqueous solutions (4.0 M): (a) left-to-right advancement of three [001] ledges with step heights of 22, 10, and 26 Å; (b) tip-induced etching of [001] ledges with 30-Å step heights to form less stable [100] ledges with step heights ranging from 3.5 to 10 Å. The tip forces used for imaging parts a and b were <10 and 40 nN, respectively.

Weaker van der Waals forces bind the bilayers together along [010]. Thus, the three well-developed faces of α-glycine each contain at least one axis where molecules interact via hydrogen bonding.

The surface topography of the (010) face of a freshly cleaved crystal of α-glycine immersed in aqueous solution saturated with glycine (3.5 M), as revealed by PMIM and AFM, consisted of terraces bounded by [001] and [100] ledges (Figure 3a). Step heights ranged from ≈1 to 200 nm, with the lower limit in good agreement with the height of a single (010) bilayer (8.9 Å). The [001] ledges predominated in solution over length scales of 1 nm to 1 mm, with relatively few [100] ledges. The regions containing both [001] and [100] ledges can be described as kinks (indicated by region A in the AFM image in Figure 3a). On the basis of the observations of large {110} and {011} faces in the macroscopic crystals, as detected by optical microscopy, it is reasonable to assign the step planes of the [001] and [100] ledges to (110) and (011), respectively. Dynamic *in situ* studies of crystal growth on the (010) face indicated that growth occurred with rapid

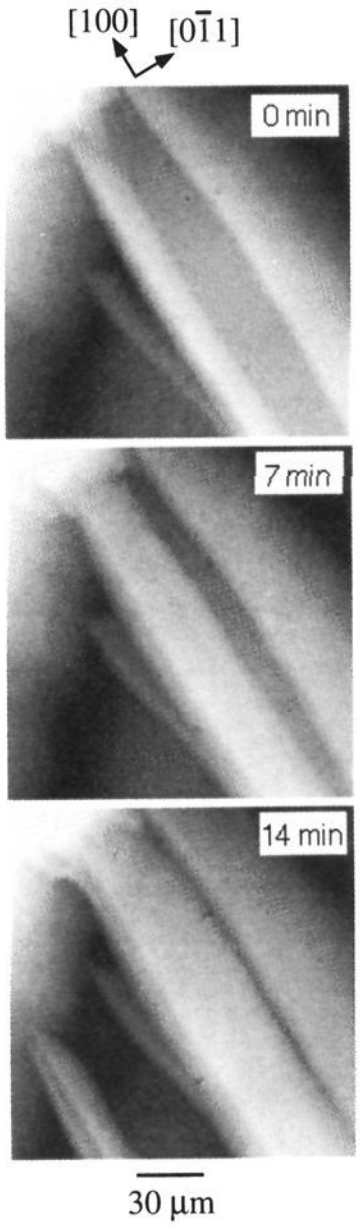

Figure 5. *In situ* PMIM of growth of the {011} terraces of the {010} face of α-glycine, illustrating ledge advancement along [100] and [0$\bar{1}$1]. At 0 min two terraces are separated by a 250-nm trough about 30-μm wide. At 7 min the trough has filled in considerably and the {011} terraces are separated by 10 μm. At 14 min the terraces have almost coalesced and are separated by less than 4 μm. In addition another terrace has formed in the lower left corner by rapid growth along the [100] axis.

advancement of [100] ledges, associated with the [001]/[100] kinks, along the [001] direction (Table 1). This was accompanied by slower [001] ledge advancement along [100] (Figure 4). Initial rates of [100] ledge advancement typically were on the order of 200 nm/s at supersaturations of ~25 ± 5% (4.3 M). The rate of [001] ledge advancement was approximately 5–10× smaller than that of [100] ledge advancement under similar growth conditions. The anisotropy in growth rates along these directions is responsible for the observed formation of the (010) terraces primarily bounded by [001] ledges. When the [001] ledge heights were less than 50 Å, the ledge advancement rates commonly differed for each ledge, resulting in ledge coalescence (Figure 4a). The slowly advancing [001] ledges gradually merged, resulting in an increase in $\lambda_{(010)}$ as well as the ledge height.

Application of large tip forces (>30 nN) resulted in tip-induced etching of [001] ledges and the progressive formation of ledges parallel to the scanning direction (Figure 4b). Step heights of 4 Å were observed, corresponding to half of a bilayer (i.e., a single hydrogen-bonded sheet). However, these ledges were not thermodynamically stable, since tip-induced etching generally required multiple scans and the surface structure *always* reverted back to one with [001] ledges under equilibrium conditions and small tip forces. The ability to mechanically fabricate thermodynamically unfavorable ledges suggests an approach to modifying local substrate topography and the corresponding adsorption characteristics, which can ultimately affect crystal growth modes in small, defined regions of the crystal.

The surface topography of the (110) face is best described as an ensemble of terraces, with ledge heights ranging from ~5 Å

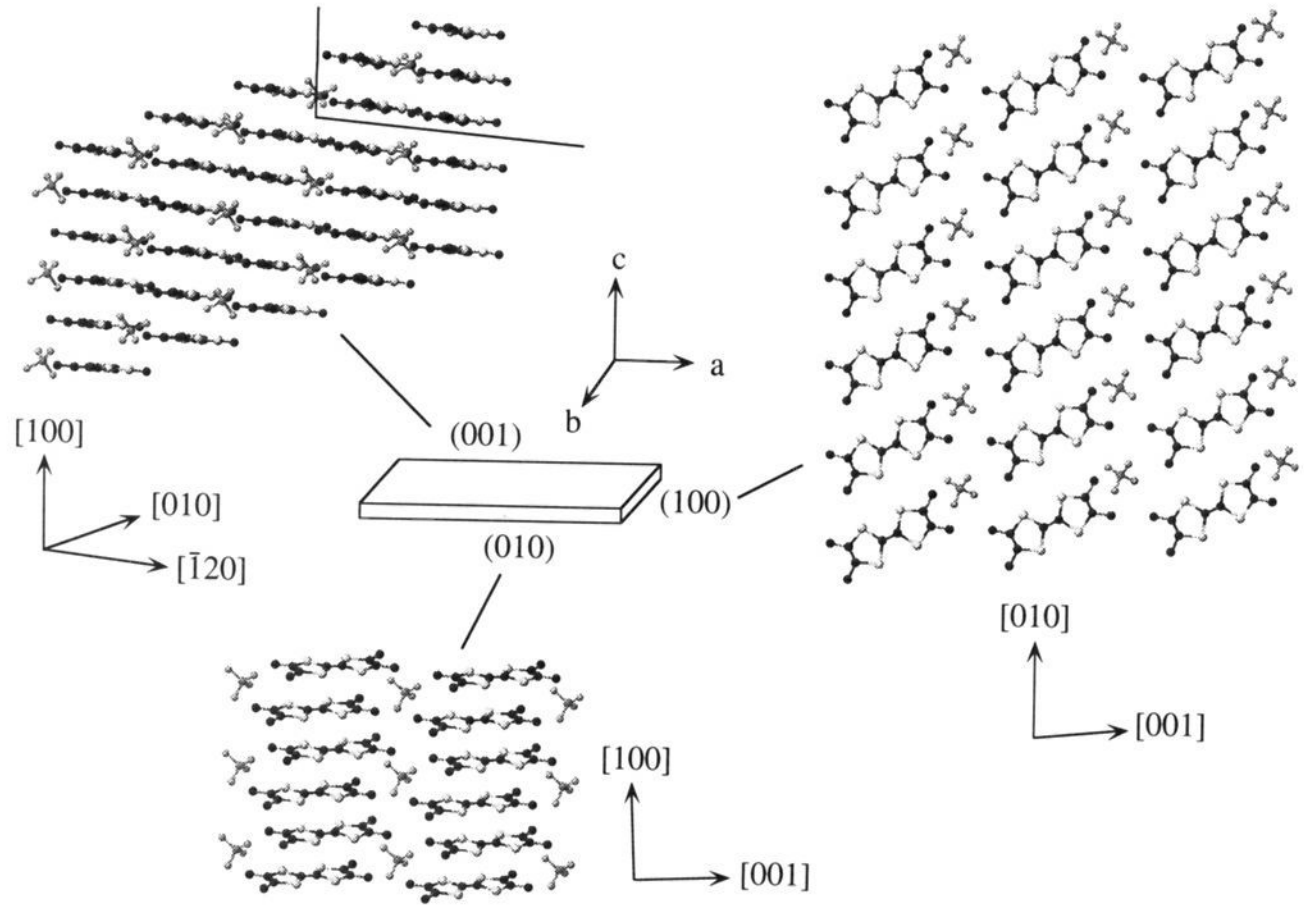

Figure 6. Schematic representation of the macroscopic crystal habit and molecular structure of $(TMTSF)_2ClO_4$. The crystal habit is described by a parallelepiped with the {001} comprising the largest exposed face. TMTSF molecules are stacked along [001]. A layered structure is also evident, with the TMTSF molecules assembled in (001) layers held together by weak van der Waals interactions along [001]. The TMTSF molecules are also organized into (210) layers, in which the molecules are held together by dispersive Se–Se interactions along the [$\bar{1}$20] direction. The [100] and [$\bar{1}$20] ledge directions forming the observed kink sites are shown by solid lines. The small area of the $(TMTSF)_2ClO_4$ crystal tip prevented determination of the plane constituting this face. However, the layered nature of the (210) plane supports its existence.

to >800 nm (Figure 3b). PMIM and AFM revealed that, near equilibrium conditions, the (110) terraces were bounded by [001] ledges. At higher supersaturation (>30 wt %), finger-like terraces advanced rapidly along [001] at rates of 10–20 nm/s, producing the familiar [001] ledges. Under conditions approaching equilibrium (3.5 M glycine) $\lambda_{(110)}$ increased as the [001] ledges merged. In contrast, the [001] ledges moved very slowly along [1$\bar{1}$0] or [$\bar{1}$11].[23]

Growth on (011), which does not contain the strongly hydrogen bonding [001] direction, was quite different from that on (110) and (010). The (011) terraces were more two-dimensional with relatively large $\lambda_{(011)}$, and [100] ledges slightly favored (Figure 3c). Dynamic PMIM measurements revealed rapid advancement of multiple (011) terraces, with ledge heights approaching 100 nm each, along [100] during the initial stages of growth. AFM measurements on well-formed terraces also indicated 100-nm ledge heights. However, it was difficult to assign the growth to a specific ledge. Growth along [100] was followed by slow advancement of [100] ledges along [0$\bar{1}$1], which served to fill in the regions between terraces (Figure 5). The rate of advancement of the leading edges of the (011) terraces along [100] was approximately 3 times the rate of [100] ledge advancement along [0$\bar{1}$1], resulting in a growth mode that was more two-dimensional than that on (010) or (110). Elliptical island growth was observed at lower supersaturations, but a terraced structure with [100] ledges evolved as these islands coalesced.

$(TMTSF)_2ClO_4$. The organic conductor $(TMTSF)_2ClO_4$ crystallizes in the triclinic space group $P\bar{1}$ (a = 7.266, b = 7.678, c = 13.275 Å, α = 84.58, β = 86.73, γ = 70.43 °).[24] The crystal

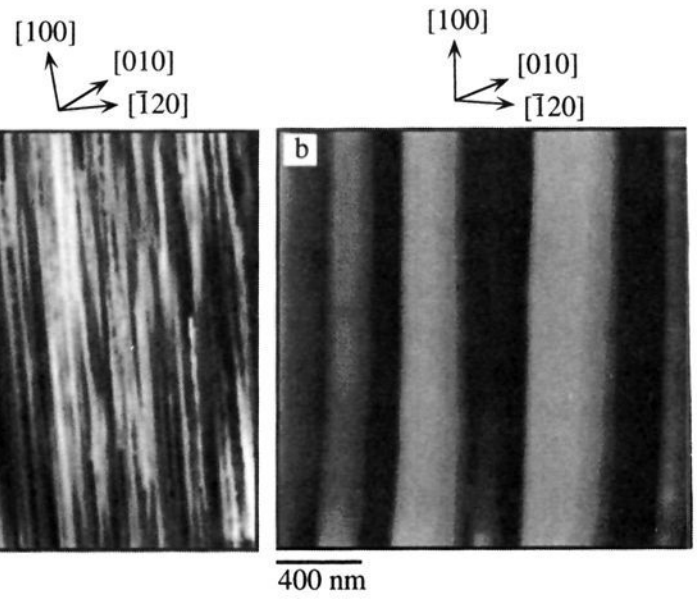

Figure 7. Surface structure of the {001} face of $(TMTSF)_2ClO_4$ in air as measured by (a) PMIM (400-nm height scale) and (b) AFM (250-nm height scale). The surfaces consists of {001} terraces intersected by ledges running along [001]. The AFM data were obtained in the constant-force mode and are unfiltered.

structure reveals segregated charge-transfer stacks of TMTSF molecules along [100], with disordered perchlorate anions contained in pockets that result from the "zig-zag" TMTSF chain motif (Figure 6). Crystals of $(TMTSF)_2ClO_4$ have a needle-like habit with the needle axis corresponding to [100], which is the direction of strong π–π charge-transfer interactions between TMTSF molecules. Weaker intermolecular interactions along [$\bar{1}$20], principally associated with polarizable selenium atoms of neighboring TMTSF stacks, and very weak van der Waals interactions along [001] between TMTSF methyl groups give rise to the respective morphological importance of the (010) and (001) faces. As a consequence of the intermolecular bonding interactions along the [001] and [$\bar{1}$20] directions, the TMTSF molecules are assembled into (001) and (210) layers, respectively. The (001) face, typically the largest in the mature crystal, was examined in this study.

(23) The direction of [001] ledge advancement was difficult to discern in this case and may be due to motion along either the [1$\bar{1}$0] or [$\bar{1}$11] direction, both of which are contained in the (110) plane. However, on the basis of the macroscopic crystal morphology, the {110} and {011} faces are joined by the ⟨111⟩ directions. It therefore is reasonable to suggest that slow advancement of the [001] ledges is along the [$\bar{1}$11] direction.

(24) (a) Bechgaard, K.; Cowan, D. O.; Bloch, A. N. *J. Chem. Soc., Chem. Commun.* **1974**, 937. (b) Bechgaard, K.; Carneiro, K.; Rasmussen, F. B.; Olsen, M.; Rindorf, G.; Jacobsen, C. S.; Pedersen, H. J.; Scott, J. C. *J. Am. Chem. Soc.* **1981**, *103*, 2440.

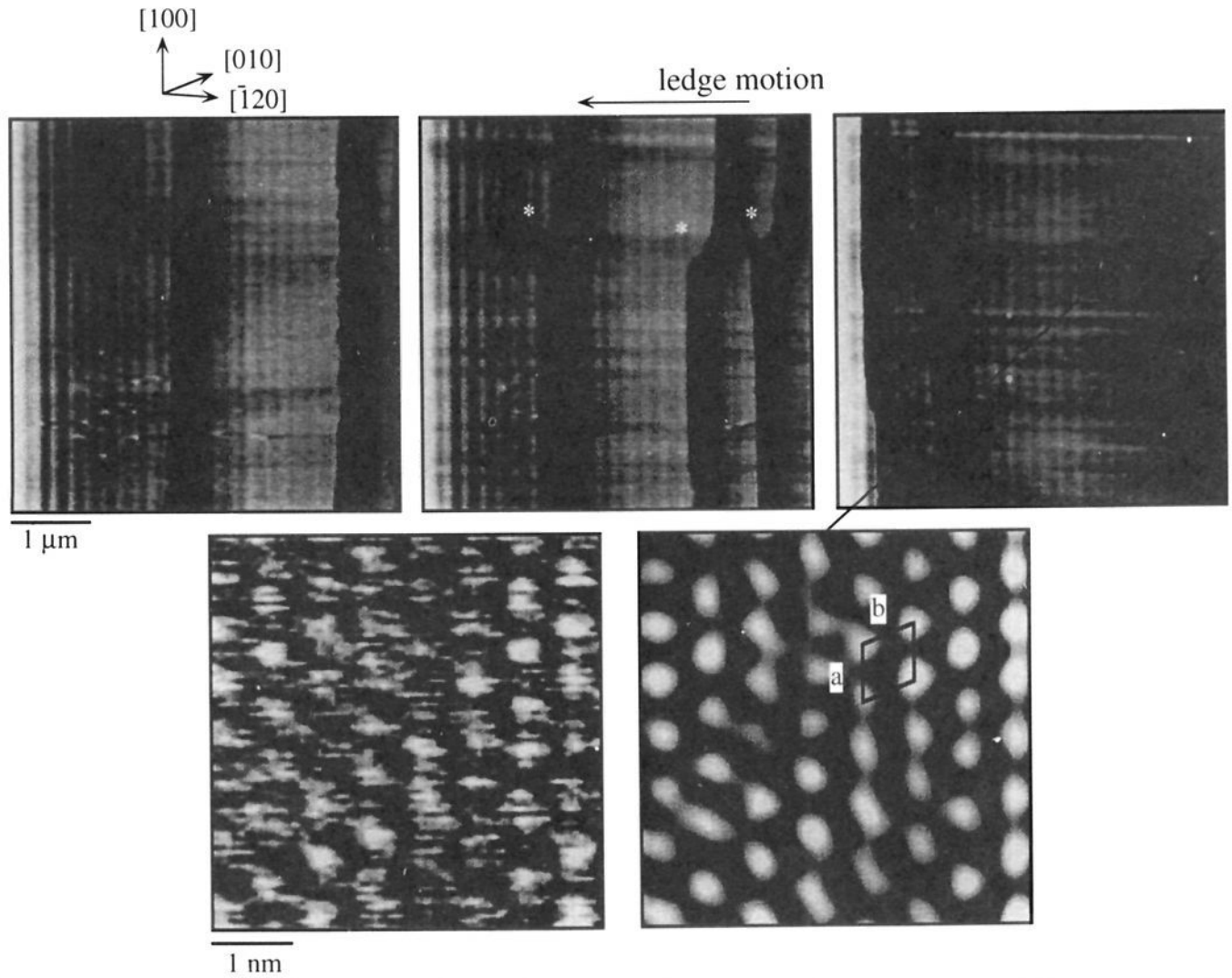

Figure 8. (a, top) *In situ* AFM of the {001} face of $(TMTSF)_2ClO_4$, showing dissolution under potential control. During dissolution (middle), [100] ledges recede along [010]. The ledge motion can be arrested by increasing the electrochemical potential to $E > E_0$ (left and right). The step heights are 1.3 nm. The AFM data were obtained in the constant-force mode and are unfiltered. The vertical ripples in the images are the result of cantilever oscillations arising from feedback and do not represent true topographic features. The entire time sequence is 90 s. (b, bottom) Molecular resolution on a flat etched region illustrating the molecular level structure of the (001) plane: (left) unfiltered data; (right) Fourier filtered image. The lattice parameters estimated from the image contrast are $a = 7.16$, $b = 7.48$ Å, and $\gamma = 67.6°$, in good agreement with those determined by X-ray crystallography ($a = 7.266$, $b = 7.678$ Å, $\gamma = 70.43°$). The bright spots correspond to either the ClO_4^- anions or TMTSF methyl groups, depending upon whether this region of the (001) face is terminated with anion or cation layers, respectively.

PMIM and AFM of the (001) face of as-grown crystals of $(TMTSF)_2ClO_4$ exhibited numerous (001) terraces bounded by [100] ledges (Figure 7). The ledge heights ranged from 20 to 100 nm, and $\lambda_{(001)}$ ranged from 200 to 400 nm. The morphology of the ledges resembled that of the mature crystal, with the ledge orientation corresponding to the TMTSF stacking direction. On the basis of the solid-state structure and the macroscopic morphology, the step plane of the [100] ledge is presumed to be (010). The observation of anisotropic terraces is evidence that $(TMTSF)_2ClO_4$ growth under electrocrystallization conditions involves fast incorporation along [100].

The roughness of the (001) face prohibited the acquisition of meaningful AFM data at the molecular scale. However, immersion of $(TMTSF)_2ClO_4$ in either ethanol or propylene carbonate resulted in a flattening of the ledge structure on (001) to give molecularly flat terraces with $\lambda_{(001)} \approx 2\ \mu m$. This process could be enhanced by electrochemical cathodic etching of $(TMTSF)_2ClO_4$ in ethanol or propylene carbonate. These experiments were performed by controlling the potential of a single crystal of $(TMTSF)_2ClO_4$, mounted in the AFM cell, in a configuration similar to that described for AFM studies of metal electrode interfaces.[25] Near equilibrium conditions the surface concentration of TMTSF is defined by the applied potential according to the Nernst equation (eq 1), where E is the

$$E = E_0 + (RT/nF) \ln(C_o/C_r) \quad (1)$$

$$(TMTSF)_2ClO_4(s) + e^- \rightarrow 2TMTSF(solution) + ClO_4^-(solution) \quad (2a)$$

$$2TMTSF(solution) + ClO_4^-(solution) \rightarrow (TMTSF)_2ClO_4(s) + e^- \quad (2b)$$

applied potential, E_0 is the reversible potential, n is the number of electrons, and C_o and C_r are the surface concentrations of oxidized and reduced species, respectively. It is important to note that changing the electrochemical potential is tantamount to changing the supersaturation at the crystal interface. This enabled control of the rate of dissolution (and growth, *vide infra*) by manipulation of the applied electrochemical potential (eqs 2a and 2b). However, electrochemical control of the interfacial potential allows for much better control of supersaturation, and the corresponding etching and growth behavior, compared to nonconductive organic crystals such as α-glycine.

At potentials more anodic than the reversible potential ($E > E_0 = 0.42$ V vs SCE), in an ethanol solution containing n-Bu_4N^+-ClO_4^-, the (001) surface of the $(TMTSF)_2ClO_4$ crystal was stable and exhibited large terraces with [100] ledges (Figure 8). The step height was typically 13.3 Å, equivalent to the c lattice parameter and corresponding to the thickness of a TMTSF layer (and its accompanying ClO_4^- anions) along the [001] direction. Changing the potential to values slightly cathodic of E_o resulted

(25) (a) Chen, C. H.; Kepler, K. D.; Gewirth, A. A.; Ocko, B. M.; Wang, J. *J. Phys. Chem.* **1993**, *97*, 7290. (b) Pan, J.; Tao, N.; Lindsay, S. M. *Langmuir* **1993**, *9*, 1556. (c) Chen, C. H.; Gewirth, A. A. *Ultramicroscopy* **1992**, *42*, 437. (d) Brown, G. M.; Thundat, T.; Allison, D. P.; Warmack, R. J. *J. Vac. Sci. Technol., A* **1992**, *10*, 3001. (e) Cruickshank, B. J.; Gewirth, A. A.; Rynders, R. M.; Alkire, R. C. *J. Electrochem. Soc.* **1992**, *139*, 2829. (f) Hendricks, S. A.; Kim, Y. T.; Bard, A. J. *J. Electrochem. Soc.* **1992**, *139*, 2818. (g) Chen, C. H.; Gewirth, A. A. *J. Am. Chem. Soc.* **1992**, *114*, 5439. (h) Chen, C. H.; Gewirth, A. A. *Phys. Rev. Lett.* **1992**, *68*, 1571. (i) Chen, C. H.; Gewirth, A. A. *J. Am. Chem. Soc.* **1992**, *114*, 451.

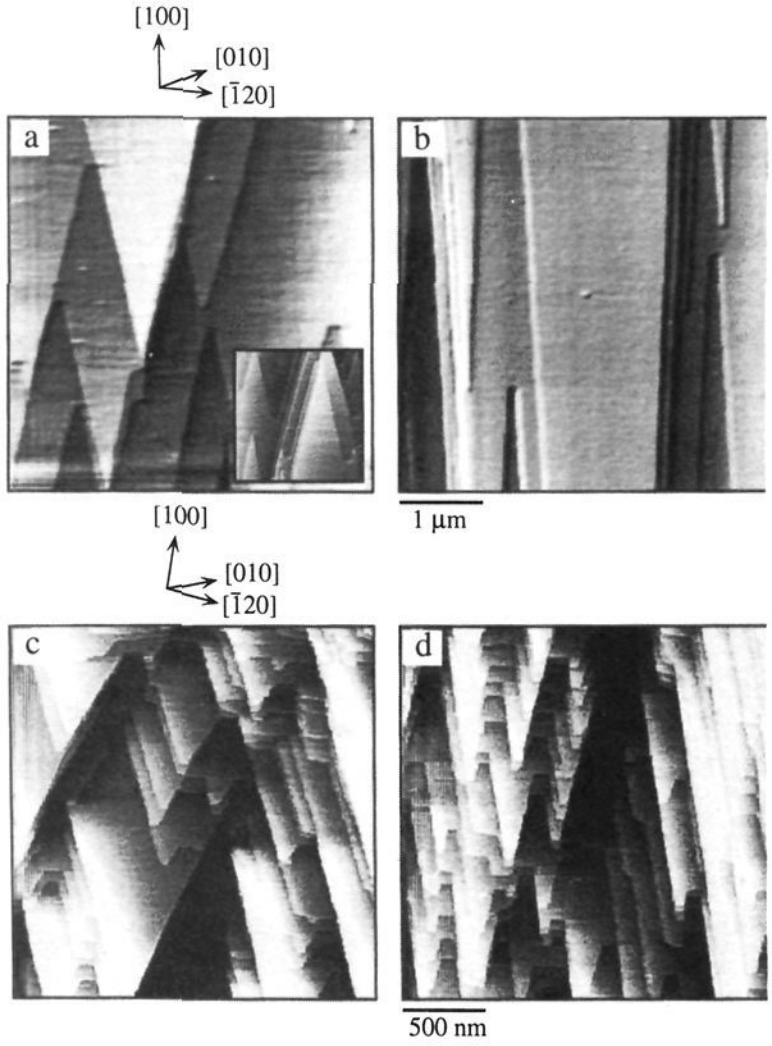

Figure 9. *In situ* AFM images of fast ledge motion on the (001) face of $(TMTSF)_2ClO_4$: (a) $E_{applied}$ = 0.42 V (vs SCE), v_t = 200 nm/s in the downward direction, 0.1 M n-$Bu_4^+ClO_4^-$/ethanol (inset: scanning in the upward direction); (b) $E_{applied}$ = 0.42 V, v_t = 381 nm/s in the downward direction, 0.1 M n-$Bu_4^+ClO_4^-$/ethanol; (c) $E_{applied}$ = 0.35 V, v_t = 105 nm/s in the downward direction, 0.1 M n-$Bu_4^+ClO_4^-$/propylene carbonate; (d) $E_{applied}$ = 0.500 V, v_t = 105 nm/s in the downward direction, 0.1 M n-$Bu_4^+ClO_4^-$/propylene carbonate. The step heights correspond to 1.3 nm in all images. The AFM data were obtained in the constant-force mode and are unfiltered.

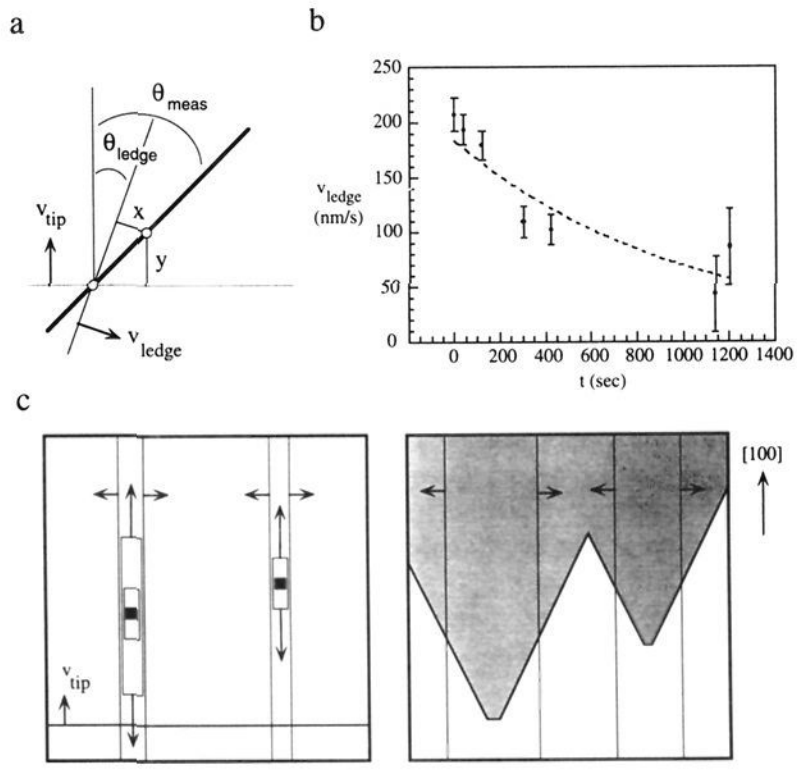

Figure 10. (a) Description of the coordinate system for measurement of ledge motion rates. (b) Experimentally measured ledge velocity versus time for the dissolution of $(TMTSF)_2ClO_4$ in ethanol. (c) Proposed dissolution mechanism for the (001) face of $(TMTSF)_2ClO_4$ that leads to triangular etching features. The left panel depicts the initial stages of rapid ledge development that result from rapid advancement of an initially formed vacancy along [100]. Once formed, the ledges move along [$\bar{1}$20]. The right panel depicts the actual [100] ledges, drawn as thin, solid vertical lines, moving horizontally along [$\bar{1}$20]. Ledges receding toward one another are manifest as triangles that point in the same direction as the vertical AFM tip scan direction, whereas ledges receding away from each other are manifest as triangles pointing in the opposite direction.

in the recession of the [100] ledges normal to the [100] direction (Figure 8, upper middle), which was the dominant mechanism for dissolution at this stage. These ledges swept aperiodically across the (001) surface, the rate increasing with increasing cathodic potential but slowing with time at a fixed potential. This process occasionally was accompanied by the formation of kinks on the [100] ledges, which, on the basis of the solid-state structure, are tentatively assigned to the formation of [$\bar{1}$20] ledges, exposing the (210) plane. Ensembles of these kink sites formed vicinal faces[26] on the [100] ledge (region denoted with * in Figure 8, *middle*). These features, also with heights of 13.3 Å and widths ranging from 10 to 50 nm, were unstable and quickly receded in the [100] direction. The relative instability of [$\bar{1}$20] ledges favors the presence of [100] ledges during the dissolution process. After electrochemical etching of the (001) surface, large (5 μm × 5 μm) molecularly flat planes emerged, allowing molecular level resolution of the (001) plane of $(TMTSF)_2ClO_4$. The periodicity of the AFM data was in good agreement with the lattice parameters of the (001) plane determined from X-ray crystallographic data and previous STM results.[27]

The images of dissolution depicted in Figure 8 were typical of those observed under conditions in which the ledge motion was slow compared to the vertical AFM tip velocity. At more cathodic potentials it is expected that the rate of ledge flow should increase due to the higher driving force for etching (faster rate of eq 2a). Indeed, multiple layers were etched simultaneously at more cathodic potentials. However, when the [100] axis of the crystal was aligned vertically, rapid ledge motion resulted in *angular* ledges rather than vertical ones. That is, the terraces now exhibited ledges tilted at an angle, θ_{meas}, with respect to the vertical scanning axis (and [100]). This observation can be attributed to [100] ledge motion that occurs on a shorter time scale than that for image acquisition, which is defined by the velocity of the AFM tip. Under fast etching conditions, the tilted ledges produced triangular features oriented along the vertical direction, the features inverting with each successive vertical scan (Figure 9). Two different orientations of the triangular features can be observed in each image; triangles pointing in the tip scan direction are higher than adjacent terraces, whereas triangles pointing opposite the tip scan direction are lower than adjacent terraces. These observations are a consequence of the relative motions of companion [100] ledges. If two [100] ledges on a given layer recede *toward* each other, they eventually annihilate one another and disappear from the surface. In this case, the triangles point in the same direction as the vertical AFM scanning direction because the terrace has a greater width at the beginning of the scan than at later times and the triangle is higher than adjacent terraces. The apex of the triangle represents the time at which that terrace has completely disappeared. However, for two [100] ledges on a given layer that originate within the frame and recede *away* from each other, the triangle points in the direction *opposite* the vertical AFM scanning direction because the newly exposed terrace, which is lower than the adjacent terraces, has a greater width at the end of the scan. The position of this apex and its width along [$\bar{1}$20] depends upon the velocity of [100] ledge motion and the distance of the original vacancy from the apex. Consequently, an apex with a smaller width signifies that less time has elapsed between vacancy formation and AFM observation. AFM images indicated a distribution of apex widths ranging from 20 to 100 nm. This vacancy, which could result from loss of a small aggregate from the (001) terrace, possesses dangling bonding sites along both the [100] and [$\bar{1}$20] directions, in the form of nanoscopic (210) and (010) step planes (Figure

(26) A vicinal face is defined as an ensemble of kinks derived from two low-index planes, generally containing strong intermolecular bonding. This ensemble forms a macroscopic plane with an orientation that depends upon the relative amounts and wavelengths of the two low-index planes.

(27) Li, S.; White, H. S.; Ward, M. D. *J. Phys. Chem.* **1992**, *96*, 9014.

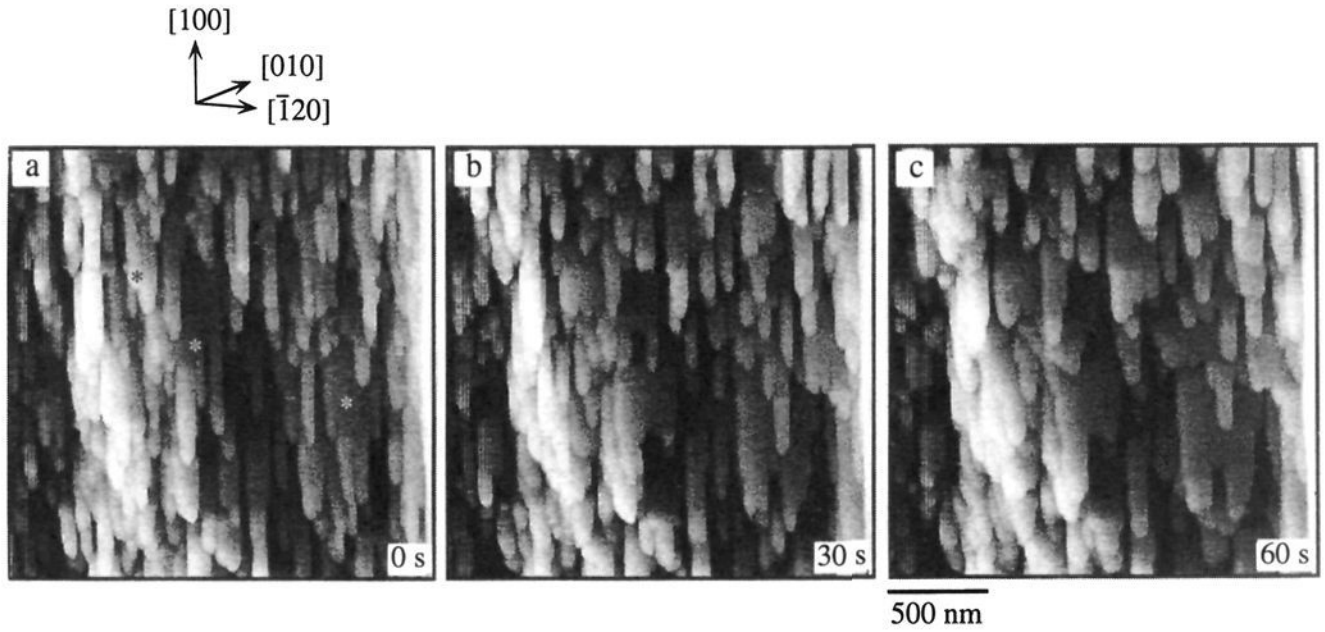

Figure 11. *In situ* AFM of the growth on the (001) face of $(TMTSF)_2ClO_4$ in a solution of propylene carbonate containing 1 mM TMTSF and 0.1 M n-$Bu_4N^+ClO_4^-$ at an applied potential of 700 mV vs SCE: (a) 0 s; (b) 30 s; and (c) 60 s. The step heights range from 1.3 to 4.0 nm, which corresponds to one to three molecular layers. The AFM data were obtained in the constant-force mode and are unfiltered.

10c). The predominance of [100] ledges can be attributed to the rapid advancement of the nanoscopic [$\bar{1}$20] ledges, and their companions, in the [100] and [$\bar{1}$00] directions. This is consistent with the large $\gamma_{(210)}$, which was also revealed in the rapid kink advancement along [100] and [$\bar{1}$00] under slow etching (*vide supra*). It is important to note, however, that observation of isosceles triangles when $\theta_{ledge} = 0°$ is conclusive evidence of [100] ledge motion at these driving forces.

Ledge velocities can be determined readily under these conditions using a simple geometric model (Figure 10a).[16a,17,28] The ledge velocity, v_{ledge}, can be determined with eq 3, in which

$$v_{ledge} = v_{tip}(\sin[\theta_{meas} - \theta_{ledge}]/\cos[\theta_{meas}]) \quad (3)$$

θ_{ledge} is the actual crystallographic angle between the ledge and the vertical axis of the crystal, θ_{meas} the observed angle between the ledge and the vertical axis of the crystal, and v_{tip} the tip velocity in the vertical direction. The value of θ_{meas}, and therefore, the aspect ratio of the triangles, will depend upon the time required for the tip to move a distance y and the ledge to move a distance x. In the limit of an infinite scan rate, the observed ledge would always correspond to the true ledge location and orientation. According to this model, θ_{meas} should increase as the vertical AFM tip velocity decreases or as the ledge motion increases, in agreement with the observed dependence on scanning rate (Figure 9a,b) or the applied potential (Figure 9c,d). It is important to note that the ledge velocities over a 20–min period of etching in ethanol were found to decrease exponentially with time (Figure 10b). This behavior can be attributed to an increasing solution concentration of TMTSF and a lower $\gamma_{(001)}$ as the roughness decreases.

Application of potentials anodic of E_o to single crystals of $(TMTSF)_2ClO_4$ in solutions containing TMTSF and n-Bu_4N^+-ClO_4^- resulted in electrocrystallization on the crystal (eq 2b). Under these conditions, AFM revealed growth on the (001) face of $(TMTSF)_2ClO_4$ (Figure 11) which occurred in a layered manner similar to that observed during etching. The fastest moving features are [$\bar{1}$20] ledges moving in the [100] direction. The [$\bar{1}$20] ledges are smaller and rougher than the [100] ledges, consistent with $\gamma_{(210)} > \gamma_{(010)}$. Rapid advancement of ledges along [100] results in the construction of (001) terraces (e.g., regions denoted by * in Figure 11). The step heights separating the terraces ranged from 13 to 40 Å, corresponding to one to three TMTSF layers. The columnar growth habit observed in these dynamic images is similar to the surface morphology of as-grown crystals (Figure 6). The rate of growth and the roughness of the terraces and ledges increase with increasing anodic potentials, consistent with greater interfacial free energies expected at higher driving forces. The observed kink sites during growth have dimensions of approximately $1.3 \times 20 \times 20$ nm^3, or approximately 520 nm^3.

(28) Although eq 3 allows calculation of ledge advancement rates based upon known and measured experimental parameters, its accuracy decreases at small θ_{meas} due to measurement errors. The uncertainty in ledge velocity, based upon an error treatment of eq 3, is quite significant at angles of θ_{meas} below 20°, where the error in calculated ledge velocity approaches 100%. However, at very small observed ledge angles, the ledge velocity can be accurately measured by observing the displacement between ledges in subsequent images. This is not possible at high etch rates because the observed ledges move quickly out of the accessible scan range.

Discussion

Energetics of Crystal Growth. AFM images of α-glycine and $(TMTSF)_2ClO_4$ interface structure were stable in fluid media at forces $\leq$10 nN, indicating that interaction of the sample with the AFM tip was minimal under these conditions. This is consistent with previous reports that AFM performed in solution eliminates capillary forces associated with thin films of atmospheric contaminants on the sample while also minimizing the attractive van der Waals forces because of the generally smaller Hamaker constant.[29] Both factors mitigate mechanical etching of the crystal interface. Furthermore, the observation that the topographical features for both α-glycine and $(TMTSF)_2ClO_4$ were identical to those observed with noninvasive PMIM indicates that the effect of the tip is not substantial at these low forces. It also is evident, however, that increasing the tip force beyond a critical value can cause destructive etching, as depicted in Figure 4.

The AFM data for near molecularly smooth α-glycine and $(TMTSF)_2ClO_4$ interfaces revealed crystallographic ledges whose step heights correspond to integral values of unit cell lengths in the direction normal to the imaged face. These ledges generally are oriented along well-defined crystallographic directions, except for cases where kink structure appears. The kinks can be attributed to the formation of other crystallographic planes with surface energies higher than that of the step plane of the dominant ledge. Notably, AFM and PMIM data reveal that the kink density and corresponding interface roughening along the ledge generally decrease as growth or etching proceed, consistent with the changes in solute concentration during these processes. In addition, the roughest ledges exhibit the fastest growth and tend to grow out of existence. This is consistent with previous crystal growth models in which growth on roughened surfaces is favored because the coordination number of the attaching aggregate is maximized and the surface free energy change is small compared to that of unroughened surfaces.

(29) (a) Weisenhorn, A. L.; Hansma, P. K.; Albrecht, T. R.; Quate, C. F. *Appl. Phys. Lett.* **1989**, *54*, 2651. (b) Ohnesorge, F.; Binnig, G. *Science* **1993**, *260*, 1451.

It is therefore clear that in these cases crystal growth does not occur by a uniform face attachment mechanism but rather by a mode resembling the TLK model in which the preferred attachment sites are those that provide the greatest reduction in the overall free energy. Near equilibrium, the structure of a crystal–solution interface is dictated by the Gibbs free energy change, ΔG, upon aggregate attachment, given by eq 4,

$$\Delta G = \Delta G_{f\text{-}s} + \Delta G_{surf} \quad (4)$$

where $\Delta G_{f\text{-}s}$ is the volume free energy change due to solidification of the adsorbed species and ΔG_{surf} is the free energy change associated with aggregate attachment to the surface. The ΔG_{surf} term includes configuration entropy, solvent entropy, and ΔE_{surf}, which is the enthalpic energy resulting from aggregate attachment to the surface (eq 5). This latter term is a function of both the

$$\Delta G_{surf} = \Delta E_{surf} - T\Delta S_{surf} - T\Delta S_{solv} \quad (5)$$

$$\Delta E_{surf} = f(\Phi_{ss},\Phi_{ff},\Phi_{sf},C_{surf}) \quad (6)$$

ad-aggregate surface concentration, C_{surf}, and the noncovalent solid–solid Φ_{ss}, fluid–fluid Φ_{ff}, and solid–fluid Φ_{sf} bonding energies (eq 6). The magnitude of interaction along a specific direction, $\phi_{ii}[uvw]$, is obtained by the projection of Φ_{ii} along that $[uvw]$ direction.

The lowest energy configuration of a surface corresponds to the minimum in eq 4 with respect to the surface concentration. For a fixed supersaturation and temperature, the minimum in ΔG_{surf} is primarily dependent upon ΔE_{surf}. In the simplest case (i.e., the Temkin model[30]), Φ_{ss}, Φ_{sf}, and Φ_{ff} are isotropic and ΔE_{surf} depends solely upon the surface coordination number and is orientation independent. *However, oriented topographic features indicate anisotropy in these terms, which is a consequence of anisotropic intermolecular bonding.* In the case of structurally anisotropic crystals, the bond energies along unique crystallographic directions ($\phi_{ss}[uvw]$ and $\phi_{sf}[uvw]$) will differ as each plane will have a unique type, orientation, and density of "dangling" chemical functionalities at the solid–fluid interface. If the anisotropy in Φ_{ss} dominates over the anisotropy in Φ_{sf}, and Φ_{ff} is independent of orientation,[31] ΔG_{surf} will be direction dependent. This will result in a surface topography that is predominantly influenced by solid-state intermolecular bonding, which generally can be surmised from the crystal structure. The most common ledges will be those having the largest values of $\phi_{ss}[uvw]$, as the step planes on these ledges will have a small surface energy $\gamma_{(h'k'l')}$. Conversely, the $(hkl)_{step}$ face exposed by a kink on this ledge will have a high surface energy $\gamma_{(hkl)}$ owing to the large $\phi_{ss}[uvw]$ normal to this plane, and aggregate attachment to this face will be highly favored. Consequently, the fastest growth direction will be parallel to the $[uvw]$ ledges, provided there is sufficient kink density to support growth along the ledge and the solvent entropic terms are comparable for each face of the aggregate and attachment site.[32]

The AFM and PMIM data for α-glycine exhibit nanoscale topography and preferred growth directions reflecting anisotropic Φ_{ss} values, with fastest growth occurring along ledges parallel to the strongest hydrogen-bonding directions. The observed growth behavior corresponds to fast attachment at ledge-attached kinks that have crystal planes containing "dangling" hydrogen bonds, leading to favorable values of ΔE_{surf} and ΔG (eqs 4 and 6). For the (010) face, short intermolecular O···N separations of 2.76 Å form strong hydrogen bonds between glycine molecules along [001], which is enthalpically favored over the weaker hydrogen bonds (O···N distances of 2.88 Å) binding glycine molecules along [100]. Therefore, the structure suggests that $\phi_{ss}[001] > \phi_{ss}[100]$, which creates a stronger driving force for molecular addition along [100], consistent with the observations. AFM and PMIM also indicate that the growth on (110) is dominated by fast advancement along the strongly hydrogen bonded [001] direction, with relatively slow movement along $[\bar{1}11]$ or $[1\bar{1}0]$, corresponding to directions in which glycine molecules interact via weak van der Waals interactions ($\phi_{ss}[001] > \phi_{ss}[\bar{1}11]$ or $\phi_{ss}[1\bar{1}0]$). Similarly, (011) terraces are dominated by [100] ledges due to $\phi_{ss}[100] > \phi_{ss}[0\bar{1}1]$, as van der Waals forces along $[0\bar{1}1]$ are not as effective for attaching molecular aggregates as the hydrogen-bonding interactions along [100]. The observation of fast growth along hydrogen-bonding directions argues against strong contributions from ϕ_{sf}, which presumably would be stronger at planes with dangling hydrogen bonds.

In the case of $(TMTSF)_2ClO_4$, the predominance of [100] ledges on the (001) face is a consequence of strong charge transfer interactions between TMTSF molecules, and a corresponding large value of $\phi_{ss}[100]$ along [100]. The relatively narrow (001) terrace widths reflect weaker dispersive contacts between selenium atoms of TMTSF molecules along $[\bar{1}20]$; that is, $\phi_{ss}[100] > \phi_{ss}[\bar{1}20]$. The van der Waals interactions between (001) layers indicates weak bonding along [001] and a small value for $\phi_{ss}[001]$. Therefore, the observed topography on the nanoscale is consistent with $\phi_{ss}[100] > \phi_{ss}[\bar{1}20] > \phi_{ss}[001]$. It is important to note that the topography of the (001) face is qualitatively identical in ethanol, propylene carbonate, or methylene chloride, suggesting a minor role for ϕ_{sf} in these solvents.

The dissolution behavior of the (001) terraces of $(TMTSF)_2ClO_4$ also reflects anisotropic ϕ_{ss} values. The recession of [100] ledges is preceded by the formation of surface vacancies (*vide supra*) that possess dangling charge-transfer bonds associated with $\phi_{ss}[100]$, which are unstable and quickly advance along [100] and $[\bar{1}00]$. The fast advancement and disappearance of these nanoscopic $[\bar{1}20]$ ledges can be attributed to $\gamma_{(210)} > \gamma_{(010)}$, which is a consequence of the stronger enthalpic interactions associated with TMTSF π–π charge-transfer interactions along [100] compared to the Se–Se interactions along $[\bar{1}20]$ ($\phi_{ss}[100] > \phi_{ss}[\bar{1}20]$). The observation of kinks with high energy $[\bar{1}20]$ ledges is attributed to excess interfacial free energy under etching conditions that results from the electrochemical potential applied to the crystal interface.

Images of growth on the (001) face indicate that aggregate attachment is favored along [100], resulting in rapid extension of the terraces along [100]. This process can occur by attachment to $[100]/[\bar{1}20]$ kink sites. Attachment to the kink can occur with no net increase in interfacial free energy (in contrast to ledge attachment), while maximizing enthalpic interaction energies by attachment to an additional crystal plane compared to attachment to a single ledge ($\phi_{ss}[100] + \phi_{ss}[\bar{1}20]$ vs only $\phi_{ss}[\bar{1}20]$). The etching and growth behavior therefore parallels the anisotropic intermolecular bonding in the solid. It is interesting to note that growth on the (001) face affords the columnar terrace structure that is observed on mature, as-grown crystals in air. However, if the crystals are immersed in solution, the terrace wavelength increases with a corresponding decrease in ledge density. This suggests that the excess interfacial free energy available during crystal growth facilitates formation of a high energy "roughened" surface with small terrace wavelengths. However, under static conditions in solvent, the topography of the (001) face spontaneously reconstructs to a surface of lower

(30) For the simple case of the Temkin model $\Delta E_{surf} = 4N[{}^1/_2(\phi_{ss} + \phi_{ff}) - \phi_{sf}]$. See: (a) Temkin, D. E. *Crystallization Processes*; Consultants Bureau: New York, 1966; p 15. (b) Bennema, P.; Gilmer, G. H. In *Crystal Growth: An Introduction*; Hartman, P., Ed.; North Holland: Amsterdam, The Netherlands, 1973; pp 263–327.

(31) Since ϕ_{ff} is a function of isotropic solvent interactions, it can be considered independent of site and orientation.

(32) It is important to note that competitive solvent interactions with the different crystal planes, and the time constants for key elementary processes, such as attachment and desorption of molecules (or aggregates), surface diffusion to ledge sites, and attachment to kink sites, also will contribute to the rates of growth and etching. These are principally kinetic factors, although they may be related to thermodynamic properties such as bonding energies in the solid state.

surface energy. This observation indicates that AFM can provide comparisons of crystal interfaces under kinetic control and thermodynamic equilibrium.

Conclusions

The foregoing results clearly illustrate that anisotropic solid-state intermolecular forces play a dominant role in defining the nanoscale topography, etching, and growth characteristics of molecular single-crystal faces. In the examples described here, the behavior is dominated by nanoscale ledge structure that is coincident with directions of strong intermolecular hydrogen bonding and charge-transfer interactions. The role of excess interfacial energy during crystal growth is evident from the distribution of terraces, ledges, and kinks that differs from that observed under equilibrium conditions. These observations indicate that the surface topography is related to the morphology of macroscopic crystals, suggesting self-similarity of morphology during the crystal growth process. This is particularly evident in the anisotropic layered growth of $(TMTSF)_2ClO_4$, for which mature crystals exhibit flat, needle-like plates. The regulation of the etching and growth of $(TMTSF)_2ClO_4$ by potential control greatly facilitates examination of these processes with AFM. This capability provides an opportunity to investigate in detail the role of solvent on interface roughening at terraces and ledges, and the relationship between roughening and crystal growth rates. It is also evident from these studies that AFM can be employed to investigate the influence of different solvents on the structure of the crystal interface, which will be especially important in determining the role of solvent in surface roughening, competitive binding of solvent to crystal interfaces, and the effect of these phenomena on crystal growth.[33] Better understanding of these details will likely lead to better control over crystal growth processes and crystal properties.

Acknowledgment. The authors gratefully acknowledge the support of the National Science Foundation (Grant NSF/DMR-9107179) and the Center for Interfacial Engineering (NSF Engineering Research Centers Program). A.C.H. would like to acknowledge the support of an Upjohn Fellowship during 1992–93.

(33) Wang, J.-L.; Leiserowitz, L.; Lahav, M. *J. Phys. Chem.* **1992**, *96*, 15.